Journal of Materials Chemistry A

PAPER

View Article Online
View Journal | View Issue

Cite this: J. Mater. Chem. A, 2017, 5, 842

Activity of pure and transition metal-modified CoOOH for the oxygen evolution reaction in an alkaline medium†

Zhu Chen,[a] Coleman X. Kronawitter,[b] Yao-Wen Yeh,[c] Xiaofang Yang,[a] Peng Zhao,[d] Nan Yao[e] and Bruce E. Koel*[a]

A new electrode structure enabling low overpotentials for the oxidation of water, based on three-dimensional arrays of CoOOH nanowires, is presented. The electrocatalytic activities of pure and M-modified cobalt oxyhydroxides (M = Ni or Mn) nanowires have been investigated in detail for the oxygen evolution reaction (OER) in an alkaline environment. The pure, Ni-, and Mn-modified nanowires, with preferentially exposed low-index surfaces, were fabricated directly on stainless steel mesh current collectors using an inexpensive and scalable chemical synthesis procedure. The unique electrode structure ensures excellent substrate–catalyst electrical contact and increases the surface area accessible to the electrolyte. The OER activity of CoOOH nanowires is shown to be significantly improved through incorporation of Ni. Specifically, optimal OER activity is obtained for CoOOH nanowires with 9.7% surface Ni content, which corresponds to four-times greater current density compared to pure CoOOH. In contrast, Mn modification of the CoOOH nanowires did not improve the OER activity. Tafel analysis suggests Ni incorporation leads to change in the OER rate-determining step based on an observed decrease in the Tafel slope. Electrochemical impedance spectroscopy reveals that Ni incorporation improves the ability of the catalysts to stabilize surface intermediates, whereas Mn incorporation impedes intermediate stabilization. This study provides new insights regarding the influence of transition metal impurities on the OER activity of CoOOH and provides a clear strategy for the optimization of CoOOH-based OER catalysts in alkaline electrolytes.

Received 30th August 2016
Accepted 13th November 2016

DOI: 10.1039/c6ta07482k

www.rsc.org/MaterialsA

Introduction

Efficient execution of the oxygen evolution reaction (OER) is required for several emerging energy conversion technologies including water splitting cells, metal air batteries, and regenerative fuel cells.[1–4] The slow reaction kinetics of OER leads to efficiency losses for devices with conventional electrodes, since large energy inputs in the form of anodic overpotentials are required. As a result, research efforts have focused on finding active and stable catalysts for OER over the past decades. To date, ruthenium and iridium oxides are considered the most active catalyst for OER in acidic and alkaline conditions.[5–7] However, the high cost and limited supply of these metals prevent their large-scale implementation in OER catalysts. Perovskite metal oxides such as $Ba_{0.5}Sr_{0.5}Co_{0.8}Fe_{0.2}O_{3-\delta}$,[2,8–10] and transition metal oxides, including Mn_3O_4,[11–14] and Co_3O_4,[15–17] have demonstrated great potential as OER catalysts. In particular, cobalt-based OER catalysts are attractive due to their high activity, earth abundance, and high stability in alkaline conditions.[16,18,19]

For Co-based oxide materials, the equilibrium Pourbaix diagram predicts the formation of OER-active cobalt oxyhydroxide (CoOOH) under relevant potentials in alkaline pH.[20] In addition, strong empirical evidence based on Raman spectroscopy[16] and X-ray absorption techniques[21] support the formation of CoOOH during OER. As a result, careful investigation of CoOOH is critical for understanding OER on cobalt-based materials as it can provide more accurate information on the reaction mechanism. Recently, Burke *et al.* have reported an OER activity trend for first row transition metal oxyhydroxides where $Ni(Fe)O_xH_y$ and $Co(Fe)O_xH_y$ were shown to exhibit the highest OER activities.[22,23] The authors concluded that CoOOH provides a conductive matrix in which the Fe ions reside and form the OER active sites at low Fe concentrations.[23] In addition to crystalline oxyhydroxides, Chemelewski *et al.* illustrated the concept of amorphous OER catalysts obtained through electrodeposition

[a]Department of Chemical and Biological Engineering, Princeton University, Princeton, NJ 08540, USA. E-mail: bkoel@princeton.edu
[b]Department of Chemical Engineering, University of California, Davis, CA 95616, USA
[c]Department of Electrical Engineering, Princeton University, Princeton, NJ 08540, USA
[d]Department of Chemistry, Princeton University, Princeton, NJ 08540, USA
[e]Princeton Institute for the Science and Technology of Materials, Princeton University, Princeton, NJ 08540, USA

† Electronic supplementary information (ESI) available: Detailed synthesis and experimental procedures, additional electron microscopy analysis, XPS fitting parameters. See DOI: 10.1039/c6ta07482k

of amorphous FeOOH, which demonstrated comparable OER activity compared to Co-borate in 1 M Na_2CO_3.[24] In a more complicated ternary system, Bates *et al.* investigated the OER activity of RANEY® Ni supported Ni–Fe–Co oxide catalysts and proposed that Co activates the formation of conductive NiOOH at low overpotential which in turn activates the Fe sites.[25] In addition, Co incorporation resulted in optimal Fe–OH/OOH bond strength—an important characteristic for OER activity.[25,26]

The aforementioned studies highlight the great potential of oxyhydroxides as OER catalysts, the complexity of binary and ternary systems, and the intricate balance between dopant concentration and OER activity. Although previous studies of electrodeposited $Co(Fe)O_xH_y$,[22,23] and NiCo layered double hydroxides[27] OER catalysts have been carried out, a detailed study of Ni- and Mn-modified CoOOH OER catalysts in alkaline media has not been reported. Modification of CoOOH by Ni and Mn are particularly interesting binary oxyhydroxide catalysts according to DFT calculations—Ni doping increases the adsorption energy of surface intermediates on β-CoOOH, whereas Mn doping decreases the adsorption energy.[28] The stabilities of surface intermediates measured in terms of adsorption energy has significant impact on the OER activity of a material. A volcano-type relationship is commonly reported for metal oxide, mixed metal oxide, and transition metal oxyhydroxide OER catalysts, where optimal activity is observed when the interaction between the catalyst and the intermediates is neither too strong nor too weak.[29,30]

Herein, we investigate the OER activity of pure and M-modified CoOOH nanowires (M = Ni or Mn) in alkaline conditions. The nanowire OER catalysts are synthesized directly on stainless steel (SS) mesh substrates, which serve as current collectors and catalyst supports. This electrode structure offers excellent electrical contact between the nanowire catalysts and the current collector as well as improves the area accessible to the electrolyte—both of which are important considerations for practical OER electrodes. The OER activity of CoOOH is greatly modified with Ni incorporation, whereas Mn modification has less impact on the activity. The effects of Ni and Mn incorporation on the OER activity are explained in terms of stability of surface intermediates during reaction. The OER activity of Ni-CoOOH reaches a maximum value at 9.7% surface Ni content and decreases when the Ni content increases further. For all Ni-modified CoOOH, the Tafel slopes are much lower compared to the pure and Mn-modified CoOOH indicating possible change in the rate-determining step for OER. The results from this study will provide additional insights for the rational design of novel nanostructured catalysts for improved OER activity.

Experimental

Synthesis of pure and modified CoOOH

CoOOH was synthesized directly onto SS mesh using a chemical bath deposition technique followed by chemical oxidation in hydrogen peroxide.[31] Briefly, 5 mmol of $Co(NO_3)_2 \cdot 6H_2O$ (Aldrich, >99.00%) and 2.5 mmol of NH_4NO_3 (Aldrich, >99.0%) were added to 35 mL of de-ionized water and 5 mL of 30 wt% ammonia (Aldrich). After stirring in air for 10 min, the solution was poured into a glass reactor bottle and pre-heated at 85 °C for 1 h. Meanwhile, a SS mesh was sequentially cleaned in acetone and de-ionized water and treated in 3 M HCl for 15 min. The SS mesh was rinsed and then added to the pre-heated Co precursor solution and the entire contents were kept at 85 °C for 12 h. The resultant material consisted of $Co(OH)_2$ nanowires on the SS mesh. To convert the $Co(OH)_2$ nanowire to CoOOH, the as-prepared $Co(OH)_2$ nanowire/SS mesh was rinsed thoroughly with de-ionized water and placed in 30 wt% H_2O_2 solution containing 6 M KOH (Aldrich, 99.99%) at 45 °C for 8 h. To synthesize Ni- or Mn-modified CoOOH, the as-prepared $Co(OH)_2$ sample was immersed for 5 h in 0.5 mM $Ni(NO_3)_2 \cdot 6H_2O$ (Aldrich, >99.99%) or 0.5 mM $Mn(NO_3)_2 \cdot 6H_2O$ (Aldrich, >97%), respectively. Immediately after impregnation, the sample was rinsed and placed into a tube furnace at 100 °C under nitrogen protection for 3 h. Following this, the Ni- or Mn-impregnated sample was subjected to the same H_2O_2 treatment to form Ni-CoOOH and Mn-CoOOH. To avoid accidental Fe incorporation, we followed the procedure outlined in the paper by Burke *et al.* and sequestered the Fe ions in the KOH solution prior to synthesis with $Co(OH)_2$ nanoparticles.[22] Six samples were studied in this work: pure CoOOH; three Ni-modified samples: Ni-CoOOH-A, Ni-CoOOH-B and Ni-CoOOH-C with increasing Ni content from samples A to C; and two Mn-modified samples: Mn-CoOOH-A and Mn-CoOOH-B with increasing Mn content from samples A to B. More detailed sample preparation procedures are included in the ESI.†

Structural characterization of pure and modified CoOOH

The CoOOH, Ni-CoOOH and Mn-CoOOH samples were characterized by scanning electron microscopy (SEM, Quanta 200 FE-ESEM) and transmission electron microscopy (TEM, Philips CM200 FEG-TEM) to investigate the morphology and crystal structures. X-ray diffraction (XRD, Bruker D8 Discover) and Raman (Horiba LabRAM Aramis) spectroscopy were used to determine the crystal structure and local crystallinity, respectively. The surface elemental composition was characterized using X-ray photoelectron spectroscopy (XPS, VG Scienta R3000) using a pass energy of 100 eV and a monochromatized Al Kα X-ray source operated at 250 W.

Electrochemical characterization of pure and modified CoOOH

Electrochemical testing was performed with a three-electrode configuration using a potentiostat (VersaStat 3, Princeton Applied Research). CoOOH, Ni-, or Mn-CoOOH samples were used as working electrodes, a Pt wire (PINE Research Instrument, AFCTR5) was used as a counter electrode and a double junction Ag/AgCl (PINE Research Instrument, RREF0024) was used as a reference electrode. Cyclic voltammetry and linear sweep voltammetry were conducted in nitrogen-saturated 0.1 M KOH from 0 to 1 V *vs.* Ag/AgCl at 50 and 1 mV s^{-1}, respectively. Electrochemical impedance spectroscopy (EIS) was carried out by applying 20 mV (peak-to-peak) AC voltage to the working

electrode under 0.6 V DC bias, and the frequency was scanned from 10 kHz to 10 mHz.

Results and discussion

Scanning electron microscopy (SEM) was used to assess the morphologies of the pure and modified CoOOH samples. The SEM images in Fig. 1 show that the CoOOH, Ni-CoOOH-A and Mn-CoOOH-A nanowires grow vertically and radially from the surface of the SS mesh. From Fig. 1 insets, there is no significant change to the morphologies of CoOOH nanowires after modification with Ni and Mn. SEM images of Mn-CoOOH-B, Ni-CoOOH-B, and Ni-CoOOH-C are included in the ESI (Fig. S1†).

Closer inspection of the SS mesh (Fig. 2) at different stages of the synthesis reveals that the SS mesh was first covered uniformly by a layer of material, as indicated by the increase in the roughness of the mesh surface. This layer of material is most likely $Co(OH)_2$ that serves as a template for the growth of nanowires. As the reaction progresses, $Co(OH)_2$ nanowires increase in length (Fig. 2b and c) and show stacking of hexagonal nanoplates in the growth direction (Fig. 2d and S2†). Additionally, Fig. S2† shows small particles found at the tip of the nanowires. This observation suggests that nanowires grow by nucleating nanoplates on the tip surfaces of existing nanowires. The average length of the pure and modified CoOOH nanowires is 10 μm and the diameters range from 250 to 500 nm. Based on the averaged dimensions of the nanowires and the SS mesh, the increase in the surface area accessible to electrolyte can be ~45 times that of a conformal thin film on the SS mesh. Assuming the same activity for nanowire surfaces and a thin film surface, this higher surface area translates into a higher current density, which is a distinct advantage of our electrode geometry.

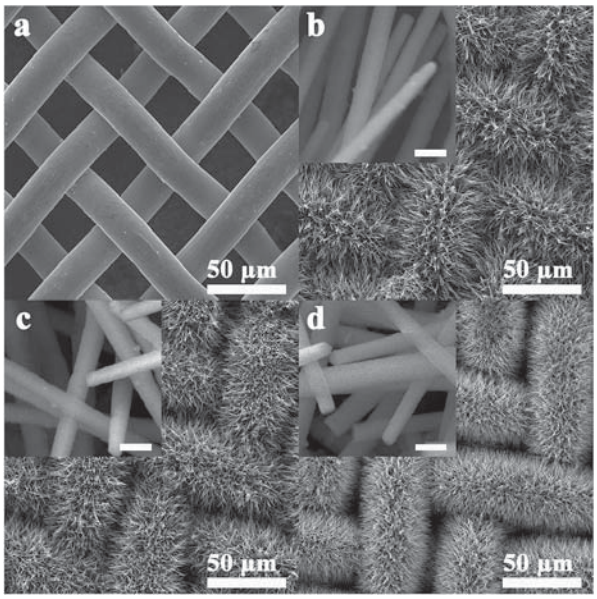

Fig. 1 SEM images of (a) clean SS mesh substrate, and (b) CoOOH, (c) Mn-CoOOH-A and (d) Ni-CoOOH-A nanowires on the SS mesh substrate. Insets show SEM images of the nanowires at a higher magnification, with scale bars to represent 500 nm.

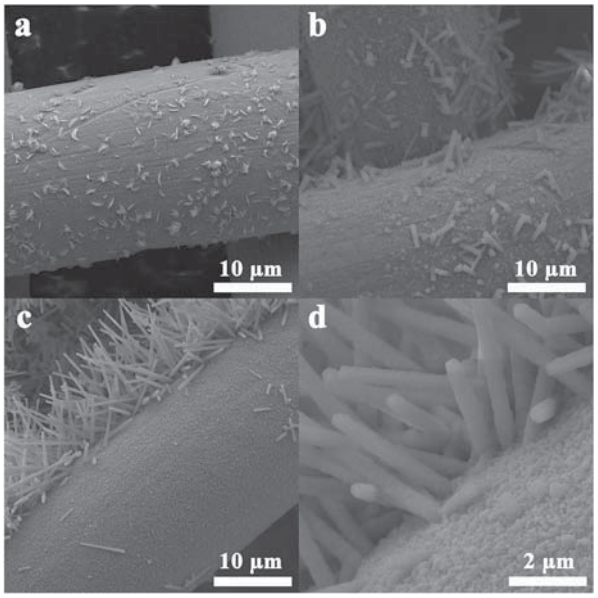

Fig. 2 SEM images of CoOOH nanowires at times (a) 0.5 h, (b) 1 h, and (c) 6 h after placing the substrate into the reaction mixture. (d) High magnification of (c) showing the nanowire–SS mesh interface.

Transmission electron microscopy (TEM) illustrates the layered structure of the nanowires, which results from stacked hexagonal nanosheets (Fig. 3) and is consistent with the SEM results. Selected area electron diffraction (SAED) was collected near the corners of the nanowires and illustrates clear diffraction spots corresponding to the {003} planes of β-CoOOH and agrees well with previous results.[32] Furthermore, the clear diffraction patterns indicate that all of the nanowires samples are highly crystalline. By measuring the distance between each of the diffraction spots, the interplanar distance of the {003} planes can be calculated. Table S1† summarizes the (003) *d*-spacing for all nanowire samples using Au nanoparticles as reference for SAED calibration. The *d*-spacing is 0.44 nm for CoOOH, which agrees with previously reported values.[32] Upon modification with Ni, the *d*-spacing increased to 0.45 nm, whereas upon modification with Mn, the *d*-spacing remained at 0.44 nm. High resolution TEM images in Fig. S3† illustrate clear crystal lattices with a *d*-spacing of 0.43–0.44 nm corresponding to the (003) planes of β-CoOOH.[32] Based on the insets of Fig. S3† that show disruptions of the lattice fringes, Mn and Ni modifications create local defects in the crystal structure of pure CoOOH. The discrepancy between the values of the (003) *d*-spacing obtained from SAED calculations and from the HR-TEM images can be due to inaccuracy in measuring the fringe spacing in the latter method. In addition, SAED is an average measurement over a larger area whereas lattice fringes are localized to a particular region. In any case, the differences in *d*-spacing values are not significant enough to reassign a different crystal structure to the nanowires.

The bulk crystal structure of the oxyhydroxide samples was investigated using XRD (Fig. 4a). However, due to the strong diffraction of X-rays from the SS mesh substrate, we were only able to identify the (003) diffraction peak of β-CoOOH at 20.2° 2θ,

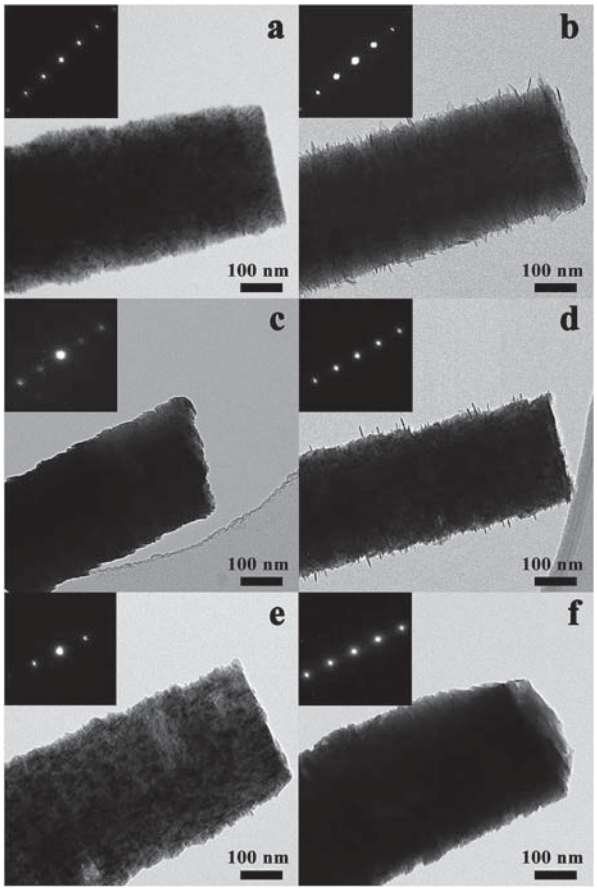

Fig. 3 TEM images of (a) CoOOH, (b) Mn-CoOOH-A, (c) Mn-CoOOH-B, (d) Ni-CoOOH-A, (e) Ni-CoOOH-B, and (f) Ni-CoOOH-C. Insets show the selected area electron diffraction patterns from the edges of the nanowire catalysts.

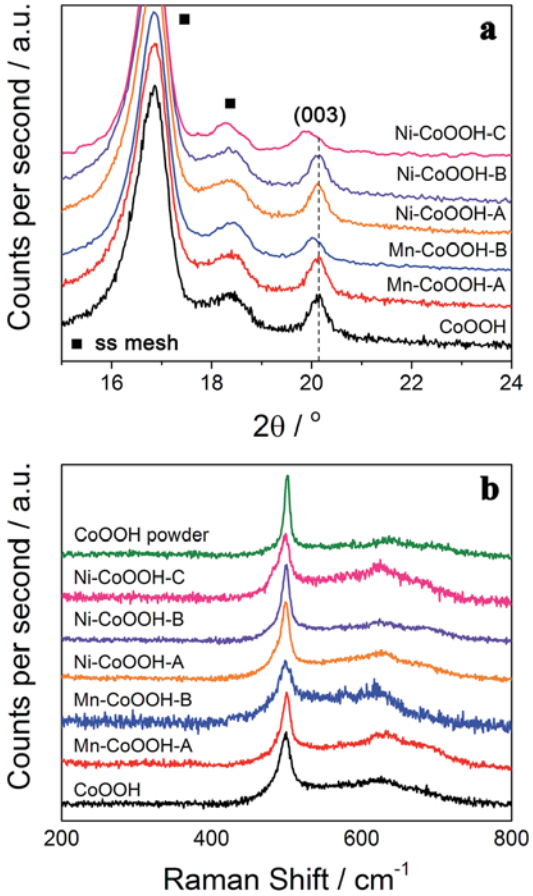

Fig. 4 (a) XRD pattern of pure, Ni- and Mn-modified CoOOH nanowires. Dashed line indicates the (003) diffraction peak. (b) Raman spectra of pure and Ni- and Mn-modified CoOOH nanowires on SS mesh. CoOOH powder was synthesized according to procedures from ref. 38.

which corresponds to a *d*-spacing of 4.39 Å. Upon Ni modification, the (003) diffraction peak intensity is shifted to 19.9° 2θ corresponding to a 1.6% increase in the *d*-spacing to 4.46 Å. With Mn incorporation, the (003) diffraction peak shifted to 20.0° 2θ indicating a smaller increase of the *d*-spacing compared to Ni modification. Based on the XRD and TEM results, it is clear that the pure and modified CoOOH nanowires are composed of β-CoOOH that has a rhombohedral crystal structure.[33,34] For the Ni-CoOOH-C sample, the XRD peak shift and the distorted peak shape could also indicate the formation of a new phase such as $Ni(OH)_2$. Based on the crystal symmetry, the nanowire growth direction is along the (001) direction, and the six exposed sides are the (100), (010), (1−10), (−100), (0−10), and (−110) planes. This is an important characteristic of our catalysts since different exposed crystal facets can possess different catalytic properties.[35–37]

A Raman scattering feature at 501 cm^{-1} is observed for all the nanowire samples (Fig. 4b), which can be assigned to be the E_g vibrational mode of β-CoOOH.[38,39] With increasing concentration of Ni and Mn, the Raman peak at 501 cm^{-1} is broadened and for Ni-CoOOH-C, which contains 15% nickel, a shoulder at lower wavenumber is observed. One possible explanation for this feature would be the presence of a small amount of NiOOH or $Ni(OH)_2$, which have Raman scattering peaks at 479 and 450 cm^{-1}, respectively.[40,41] This explanation is consistent with the observation that this shoulder is only seen for the Ni-rich sample. Segregation of different crystalline phases has also been observed in the binary oxyhydroxide system.[22] At low Ni concentration, Ni can be dispersed in the CoOOH matrix, but as the Ni concentration approaches the solubility limit in CoOOH, excess Ni could nucleate and form NiOOH or $Ni(OH)_2$ leading to a weak Raman scattering feature. We rule out the appearance of a Co_3O_4 phase, which has a Raman peak at 480 cm^{-1}, because the dominant peak for this phase at 691 cm^{-1} is not observed.[38] At higher Ni and Mn concentrations, the intensity of the E_g peak at 501 cm^{-1} decreases, which can be attributed to the distortion of the rhombohedral structure of β-CoOOH due to Ni and Mn incorporation. Another explanation for the weaker Raman peak at 501 cm^{-1} could be the change in the polarizability of the E_g vibrational mode with Ni and Mn substitution into Co sites. Additional discussions are included in the ESI.†

X-ray photoelectron spectroscopy (XPS) was used to investigate the elemental composition of the catalyst surfaces. These results are shown in Table S2.† Elemental compositions (Table S3†) obtained from energy dispersive X-ray spectroscopy (EDX),

are similar, which indicates fairly homogeneous Ni and Mn concentrations, but with perhaps slightly higher Ni and Mn concentrations near the nanowire surface. The XPS spectra of the Co $2p_{3/2}$, Ni $2p_{3/2}$, Mn $2p_{3/2}$ and O 1s regions are shown in Fig. 5. The Co $2p_{3/2}$ spectra of pure and modified CoOOH showed similar spectral features, which is expected as the oxidation of cobalt should remain as Co^{3+} for all the nanowire samples (Fig. S4†). The overall line shape or envelope in such Co $2p_{3/2}$ spectra arises from multiplet splitting peaks with principle lines between 780.2 and 780.4 eV, as determined by previous XPS results.[38] Clear satellite features in the Co $2p_{3/2}$ region are located 10 eV above the principle line and the line shapes of Co 2p spectra confirm Co^{3+} as the major oxidation state of cobalt in all nanowire samples.[38] Additional analysis of the Co LMM region is shown in the ESI (Fig. S5†). The O 1s signal provides further information on the chemical composition of pure and modified CoOOH. The O 1s spectrum is decomposed into four components at 529.8, 530.9, 531.9, and 532.5 eV, which corresponds to lattice O, lattice OH, adsorbed OH, and surface O–C=O from adventitious contamination, respectively. The assignments of different components of the O 1s spectra agree with previously reported results on cobalt oxyhydroxide[38] and transition metal-doped cobalt oxides.[42–44] Detailed fitting parameters used for the O 1s spectra decomposition are provided in Table S4.†

From the O 1s XPS spectra of CoOOH (Fig. 5), the ratio O : OH is 1 : 0.95 which agrees well with the stoichiometry of oxyhydroxides where an equal number of O and OH constitutes the crystal structure. Upon Ni modification, the O : OH ratio is 1 : 0.90, 1 : 0.96 and 1 : 1.9 for samples containing 5.5%, 9.7% and 15% Ni, respectively. The Ni-CoOOH-A and Ni-CoOOH-B samples contain lower surface Ni content and exhibit similar O 1s lineshapes compared to the pure CoOOH nanowires. This suggests that a similar chemical environment exists for Co ions in pure and low-Ni-concentration samples. However, Ni-CoOOH-C, which contains 15% Ni, shows a very different distribution of surface oxygen groups where lattice OH is the dominant species. A high concentration of lattice OH can result from the formation of a small amount of NiOOH or $Ni(OH)_2$ as discussed earlier in the context of the shoulder in the Raman spectrum, and therefore our XPS results agree with this assignment. In the case of Mn-incorporated samples, the O : OH ratio is 1 : 0.84 and 1 : 0.74 for 2.5% and 6% Mn-containing samples, respectively.

Ni $2p_{3/2}$ XPS spectra decomposition was carried out in accordance with the paper by Grosvenor *et al.*[45] The oxidation state of Ni and the local structure around Ni ions greatly influence the overall Ni $2p_{3/2}$ peak position and lineshape. The principle peak of Ni $2p_{3/2}$ for the Ni-modified CoOOH nanowires is located at 855.3 eV, which matches closely with the binding energy for $Ni(OH)_2$ and NiOOH, but is much higher than that for NiO. In addition, the Ni $2p_{3/2}$ spectrum of NiO is characterized by the existence of a shoulder 1.8 eV above the principle line, which is not observed in any of our Ni-containing samples. As a result, we conclude that Ni-modified CoOOH samples contain Ni^{2+} and Ni^{3+} ions similar to those found in $Ni(OH)_2$ and NiOOH. Mn $2p_{3/2}$ XPS spectra decomposition was carried out in accordance with the paper by Nesbitt *et al.*[46] By comparing to the spectrum of MnO, the lack of satellite peaks at 648 eV eliminates the possibility of Mn^{2+} in our samples. Mn^{3+} and Mn^{4+} both contribute to the broad Mn $2p_{3/2}$ peak located at 642.8 eV. Oxides and oxyhydroxides containing Mn^{3+} and Mn^{4+} possess a large diversity of crystal structures and polymorphs. Consequently we were not able to identify the structure of MnO_x or MnOOH in Mn-CoOOH-A and Mn-CoOOH-B.

Electrochemical tests of the pure and modified CoOOH nanowires were performed using a three-electrode setup. Based on the linear sweep voltammetry (LSV), analyzed on a potential scale corrected for ohmic losses, the maximum current density of Ni-CoOOH-A is 99% greater than pure CoOOH and the potential required to attain 10 mA cm^{-2} is decreased by 20 mV (Fig. 6a). With increasing surface Ni concentration, the OER

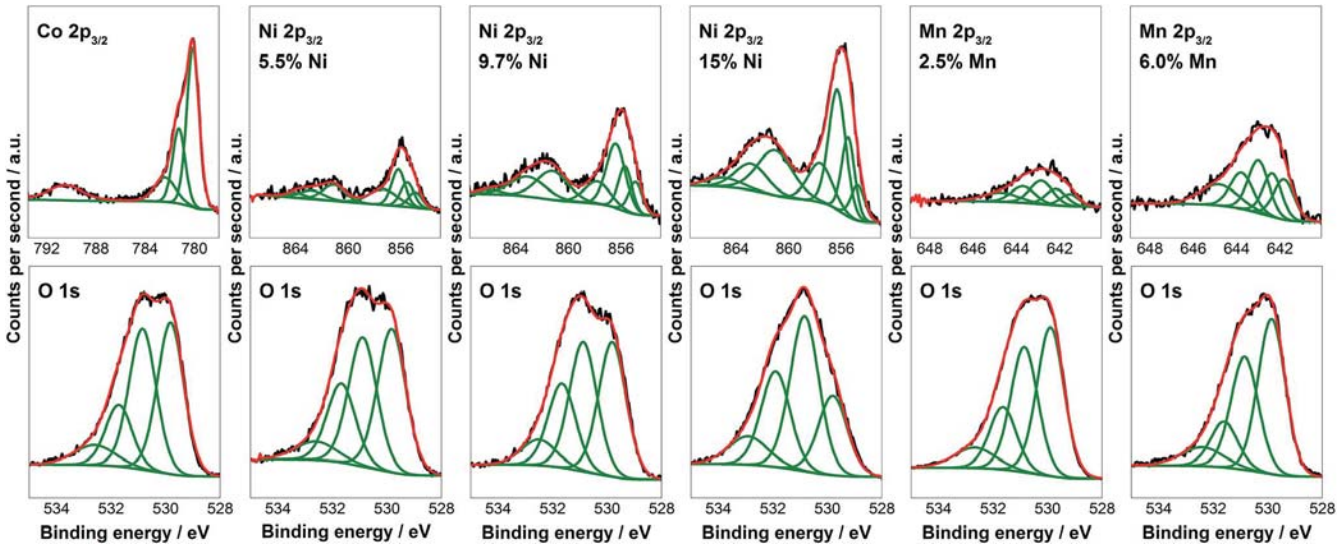

Fig. 5 XPS scans of the O 1s, Co $2p_{3/2}$, Ni $2p_{3/2}$, and Mn $2p_{3/2}$ regions of all nanowire catalysts. From left to right: CoOOH, Ni-CoOOH-A, Ni-CoOOH-B, Ni-CoOOH-C, Mn-CoOOH-A, and Mn-CoOOH-B.

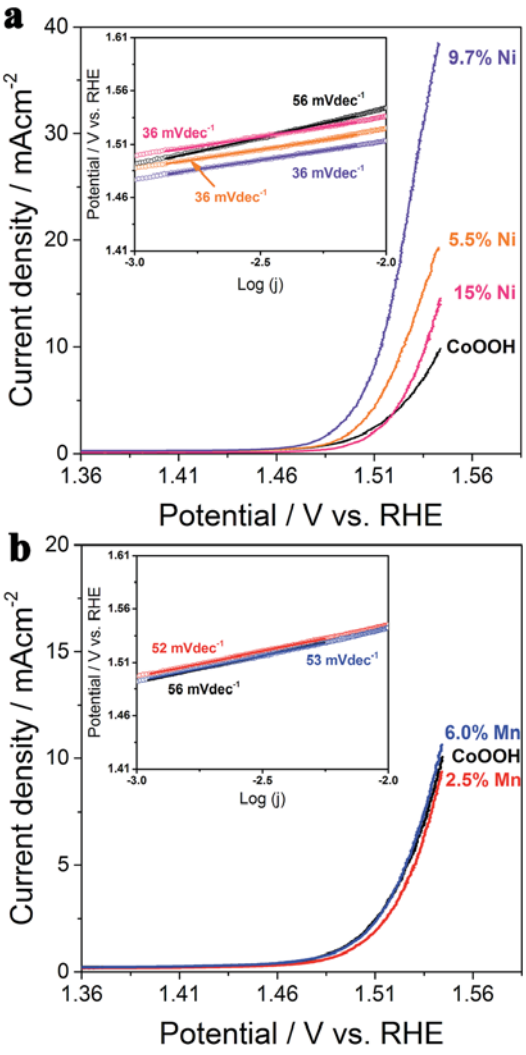

Fig. 6 Linear sweep voltammetry (corrected for ohmic losses) for (a) CoOOH and Ni-modified CoOOH and (b) CoOOH and Mn-modified CoOOH. Insets show corresponding Tafel plots.

activity increased to 400% at 1.55 V for 9.7% Ni compared to pure CoOOH. In addition, the potential at 10 mA cm^{-2} was decreased by 30 mV. However, increasing the surface Ni concentration to 15% caused a decrease in OER activity from the optimal value. Ni-CoOOH-C with 15% surface Ni has lower activity than that for 5.5% Ni, but exhibits higher activity than pure CoOOH. The OER activity of Ni-CoOOH samples are compared to NiO_xH_y nanoparticles in Fig. S7,† which clearly illustrates that Ni-modification of CoOOH creates more active OER sites than does CoOOH or NiO_xH_y alone. Based on XPS and Raman results, we conclude that NiOOH or $Ni(OH)_2$ forms on the surface of the nanowires at higher Ni concentrations and this would decrease the number of highly active sites and lead to a decrease in OER activity compared to the other Ni-modified samples. In contrast, Mn modification showed neither improvement nor decrease in the OER activity of pure CoOOH at all levels of Mn incorporation (Fig. 6b). Previous studies of a related material, Mn-doped Co_3O_4, showed a decrease in the OER activity with increasing Mn doping.[47,48] Several studies have found that Mn^{4+} ions are inactive for OER.[12,14] Recently, Smith *et al.* showed that tetragonally-distorted $Mn^{3+}O_6$ sites are very important for the OER activity of Mn-based catalysts. The apparent null influence of Mn incorporation on the OER activity in our work can be explained by the formation of both inactive Mn^{4+} and active Mn^{3+} ions from Mn incorporation.

It was recently brought to the attention of the community that incidental Fe doping was the actual reason for the improved OER activity of certain Co/Ni oxide or oxyhydroxide catalysts, according to the paper by Burke *et al.*[22] To take this into consideration, we carefully scavenged Fe ions in the KOH solutions used in all stages of the synthesis and electrochemical testing according to Burke *et al.*[22] We also believe that any trace Fe that remained in the solution would have affected all samples equally. Based on the theory that Fe is the real active sites for oxyhydroxide catalysts, all the oxyhydroxide samples would show similar activity, which is not what we observed. Additional XPS analysis regarding trace Fe concentration is included in the ESI (Fig. S5†). Furthermore, Burke *et al.* have shown that the Tafel slope of CoOOH changes from 60 to 39 mV dec^{-1} with Fe doping, which is not observed for our catalysts (see sections below).[22] As a result, we believe that the trends in OER activity reported here are due to Ni and Mn incorporation as opposed to accidental Fe doping.

Inspection of the Tafel regions in LSV of Ni- and Mn-CoOOH samples reveals a decrease in the Tafel slope for Ni-CoOOH compared to pure CoOOH (Fig. 6a inset), but no change was observed upon Mn modification (Fig. 6b inset). Pure CoOOH has a Tafel slope of 53 mV dec^{-1}, which is close to 60 mV dec^{-1}, the value commonly observed for metal oxide OER catalysts.[49–51] However, upon Ni modification, the Tafel slope decreased to 36 mV dec^{-1} and importantly this decrease was independent of Ni concentration. A decrease in the value of the Tafel slope of CoOOH catalysts have been observed by Burke *et al.*, where Fe concentrations from 33% to 79% lead to a change in the Tafel slope from 62 to 26–39 mV dec^{-1}.[22] However, these authors reported a continuous decrease in the Tafel slope for increasing Fe content,[22] which differs from our observation of a Ni concentration-independent Tafel slope.

In the literature, a change in Tafel slope has been related to several factors. First, it is suggested to imply a change in the rate-determining step of the electrochemical reaction. In this interpretation, for a Tafel slope of 60 mV dec^{-1}, the rate-determining step is a chemical step preceded by a facile one-electron transfer reaction. For a Tafel slope of 40 mV dec^{-1}, the second electron transfer is the rate-determining step. A change in Tafel slope has also been suggested to be closely tied to electrode conditioning. Doyle and Lyons suggest that a Tafel slope of 60 mV dec^{-1} is indicative of a dehydrated film, whereas a Tafel slope of 40 mV dec^{-1} represents a hydrated film.[49,52] In addition, these authors commented that the Tafel slope can change between the two values depending on electrode history, such as the aging time in KOH and/or extensive polarization experiments.[49,52] In our study, pure and Ni-modified CoOOH electrodes underwent the same chemical treatments and electrochemical conditioning. This leads us to conclude that a change in the rate-determining step is a possible reason for

the change in Tafel slope upon Ni modification. In stark contrast, Mn modification did not alter the Tafel behavior of CoOOH, which is be expected based on the insensitivity of the OER rate to Mn composition.

Electrochemical impedance spectroscopy (EIS) was performed to generate further mechanistic information. Fig. 7 and 8 display Nyquist plots corresponding to pure and modified CoOOH. The impedance data was fitted using an equivalent circuit model (insets of Fig. 7 and 8) proposed by Swierk *et al.*, where R_Ω represents the uncompensated solution resistance and contact resistance, Q_{dl} represents the double layer capacitance, R_P represents the overall resistance of OER and incorporates the charge transfer resistance associated with all faradaic steps of OER, R_S represents the formation of surface intermediates, and Q_φ represents the change in charged surface species.[53] It should be noted that the capacitive components are modelled with constant phase elements, which accounts for surface inhomogeneity and allows for proper fitting of the depressed semicircle characteristics in Fig. 7 and 8. Table S5† summarizes the optimized values of the different circuit elements.

For pure and modified CoOOH samples, the R_Ω value is ~15 Ω indicating similar overall contact resistances. For Ni concentrations of 5.5%, 9.7%, and 15%, the R_P value is decreased by 37%, 54%, and 23%, respectively. Smaller values of R_P indicate lower charge transfer resistances for OER, which can explain the improved OER activity and decreased Tafel slopes for Ni-CoOOH-A, Ni-CoOOH-B, and Ni-CoOOH-C. Another important parameter used in modelling the impedance data is R_S, which describes the relative ease of stabilizing surface species. With Ni incorporation, the R_S values are decreased by 47%, 70%, and 36% for Ni-CoOOH-A, Ni-CoOOH-B and Ni-CoOOH-C, respectively. Therefore, based on this EIS analysis, Ni incorporation also increases the catalyst's ability to stabilize surface species during the OER, in addition to lowering the charge transfer resistance. In the case of Mn doping, the values of R_P are slightly lowered upon modification of CoOOH by Mn. At 2.5% and 6% Mn content, the value of R_P decreased by

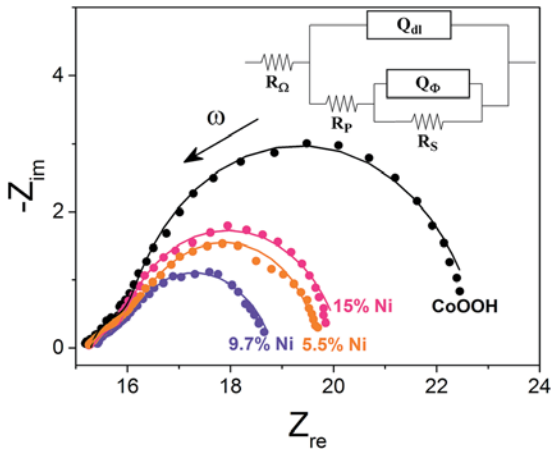

Fig. 7 Nyquist plots from EIS for pure and Ni-modified CoOOH with varying Ni content. Inset shows the equivalent circuit used for modeling.

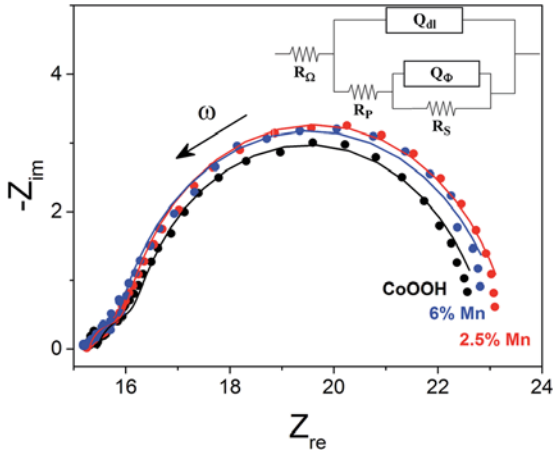

Fig. 8 Nyquist plots from EIS for pure and Mn-modified CoOOH with increasing Mn content. Inset shows the equivalent circuit used for modeling.

0.1 and 0.2 Ω, respectively. However, the values of R_S are increased by 12% for both Mn-modified samples. Higher value of R_S indicates greater difficulty in stabilizing surface species. According to these EIS results, we conclude that Ni-modified CoOOH leads to more stable adsorbed species compared to Mn-modified CoOOH, and the ability of pure CoOOH nanowires to stabilize surface intermediates falls in between the two.

Bajdich *et al.* performed first-principles calculations to investigate the effects of dopants on the adsorption energies of OH and O on the surface of CoOOH.[28] These DFT results revealed increased adsorption energies of surface species on Ni-doped CoOOH surfaces, which agrees very well with the trend observed in our EIS analysis, where decreasing R_S values are associated with Ni incorporation. Furthermore, Bajdich *et al.* predicted an overall decrease in the overpotential of the rate-determining step with Ni doping.[28] The trends we observed in OER activity and Tafel slope directly supports this prediction as well. Our electrochemical results illustrate that OER activity has a maximum around 9.7% Ni content, but this was not considered by these DFT calculations. With respect to Mn incorporation, increased R_S values correlate well with the decrease in adsorption energies of surface species predicted by Bajdich *et al.* However, these DFT calculations predicted an increase in the overpotential with Mn doping, which was not observed in our electrochemical results. This disagreement may be because these DFT calculations only considered a single type of active site involving Mn and simulate catalysis through the modelled sites with 100% probability, not accounting for lower probability reactions through higher energy pathways. As a result, the presence of multiple types of active sites might explain the discrepancy between our measured electrochemical performance and these DFT calculations for Mn modification.

Catalyst stability is an important parameter to consider for commercial application. Chronopotentiometry was performed to investigate the performance of these catalysts over time by measuring the change in potential required to obtain a 10 mA cm^{-2} current density. The catalyst structure and chemical composition were also investigated using XRD, Raman spectroscopy, and XPS

analysis after stability testing to obtain information on degradation mechanisms. The chrono-potentiometry results (Fig. S8†) show that only a 2–3% increase in the potential was observed over 25 h for the CoOOH, CoOOH with 9.7% Ni, and CoOOH with 2.5% Mn catalysts. This small increase in potential reflects the excellent stability of the tested catalysts. Consistent with these results, XRD and Raman results (Fig. S9a and b†) indicate no significant change to the catalyst structure during these tests. XPS results (Fig. S9c and d†) also indicate similar elemental composition, and Ni and Mn oxidation states, before and after stability testing.

Conclusions

A new, efficient electrode structure for the oxidation of water, based on three-dimensional arrays of CoOOH nanowires, was presented. The effects of Ni and Mn incorporation on the OER activity of CoOOH nanowire catalysts were investigated in detail. The pure, Ni-, and Mn-modified nanowires, with preferentially exposed low-index surfaces, were fabricated directly on stainless steel mesh current collectors using an inexpensive and scalable chemical synthesis procedure. The electrodes possess excellent electrical conductivity and contain no polymeric binder. The OER activity of CoOOH increased with Ni incorporation, with four times greater OER current density achieved with 9.7% Ni content. In contrast, Mn incorporation was found to have no effect on OER activity at all levels of Mn concentration. Tafel analysis indicated a possible change in the rate-determining step of OER for Ni-modified samples. EIS analysis of pure and modified CoOOH catalysts revealed that OER activity can be directly correlated with the ability to stabilize surface species, which agrees well with DFT calculations in the literature. Our study provides new insights regarding the incorporation of transition metals on the OER activity of CoOOH and illustrates stabilization of surface species as a clear strategy for optimization of CoOOH catalysts for OER in alkaline medium.

Acknowledgements

Z. C. acknowledges support by a Natural Sciences and Engineering Research Council of Canada (NSERC) Postgraduate Scholarship. This material is based upon work supported by the National Science Foundation under Grant No. CHE-1465082.

References

1 H. Inoue, T. Shimada, Y. Kou, Y. Nabetani, D. Masui, S. Takagi and H. Tachibana, *ChemSusChem*, 2011, **4**, 173–179.
2 J. Suntivich, K. J. May, H. A. Gasteiger, J. B. Goodenough and Y. Shao-Horn, *Science*, 2011, **334**, 1383–1385.
3 S. D. Song, H. M. Zhang, X. P. Ma, Z. G. Shao, R. T. Baker and B. L. Yi, *Int. J. Hydrogen Energy*, 2008, **33**, 4955–4961.
4 L. X. Zhang, S. L. Zhang, K. J. Zhang, G. J. Xu, X. He, S. M. Dong, Z. H. Liu, C. S. Huang, L. Gu and G. L. Cui, *Chem. Commun.*, 2013, **49**, 3540–3542.
5 Y. Lee, J. Suntivich, K. J. May, E. E. Perry and Y. Shao-Horn, *J. Phys. Chem. Lett.*, 2012, **3**, 399–404.
6 T. Reier, M. Oezaslan and P. Strasser, *ACS Catal.*, 2012, **2**, 1765–1772.
7 K. Sardar, E. Petrucco, C. I. Hiley, J. D. B. Sharman, P. P. Wells, A. E. Russell, R. J. Kashtiban, J. Sloan and R. I. Walton, *Angew. Chem., Int. Ed.*, 2014, **53**, 10960–10964.
8 K. J. May, C. E. Carlton, K. A. Stoerzinger, M. Risch, J. Suntivich, Y. L. Lee, A. Grimaud and Y. Shao-Horn, *J. Phys. Chem. Lett.*, 2012, **3**, 3264–3270.
9 B. R. Wygant, K. A. Jarvis, W. D. Chemelewski, O. Mabayoje, H. Celio and C. B. Mullins, *ACS Catal.*, 2016, **6**, 1122–1133.
10 A. Grimaud, K. J. May, C. E. Carlton, Y. L. Lee, M. Risch, W. T. Hong, J. G. Zhou and Y. Shao-Horn, *Nat. Commun.*, 2013, **4**, 2439.
11 Y. Gorlin, B. Lassalle-Kaiser, J. D. Benck, S. Gul, S. M. Webb, V. K. Yachandra, J. Yano and T. F. Jaramillo, *J. Am. Chem. Soc.*, 2013, **135**, 8525–8534.
12 D. M. Robinson, Y. B. Go, M. Mui, G. Gardner, Z. J. Zhang, D. Mastrogiovanni, E. Garfunkel, J. Li, M. Greenblatt and G. C. Dismukes, *J. Am. Chem. Soc.*, 2013, **135**, 3494–3501.
13 C. H. Kuo, I. M. Mosa, A. S. Poyraz, S. Biswas, A. M. E-Sawy, W. Q. Song, Z. Luo, S. Y. Chen, J. F. Rusling, J. He and S. L. Suib, *ACS Catal.*, 2015, **5**, 1693–1699.
14 P. F. Smith, B. J. Deibert, S. Kaushik, G. Gardner, S. J. Hwang, H. Wang, J. F. Al-Sharab, E. Garfunkel, L. Fabris, J. Li and G. C. Dismukes, *ACS Catal.*, 2016, **6**, 2089–2099.
15 J. D. Blakemore, H. B. Gray, J. R. Winkler and A. M. Muller, *ACS Catal.*, 2013, **3**, 2497–2500.
16 B. S. Yeo and A. T. Bell, *J. Am. Chem. Soc.*, 2011, **133**, 5587–5593.
17 J. A. Koza, Z. He, A. S. Miller and J. A. Switzer, *Chem. Mater.*, 2012, **24**, 3567–3573.
18 P. W. Menezes, A. Indra, D. Gonzalez-Flores, N. R. Sahraie, I. Zaharieva, M. Schwarze, P. Strasser, H. Dau and M. Driess, *ACS Catal.*, 2015, **5**, 2017–2027.
19 D. U. Lee, J. Y. Choi, K. Feng, H. W. Park and Z. W. Chen, *Adv. Energy Mater.*, 2014, **4**, 1301389.
20 J. Chivot, L. Mendoza, C. Mansour, T. Pauporte and M. Cassir, *Corros. Sci.*, 2008, **50**, 62–69.
21 A. Bergmann, E. Martinez-Moreno, D. Teschner, P. Chernev, M. Gliech, J. F. de Araujo, T. Reier, H. Dau and P. Strasser, *Nat. Commun.*, 2015, **6**, 8625.
22 M. S. Burke, M. G. Kast, L. Trotochaud, A. M. Smith and S. W. Boettcher, *J. Am. Chem. Soc.*, 2015, **137**, 3638–3648.
23 M. S. Burke, S. H. Zou, L. J. Enman, J. E. Kellon, C. A. Gabor, E. Pledger and S. W. Boettcher, *J. Phys. Chem. Lett.*, 2015, **6**, 3737–3742.
24 W. D. Chemelewski, H. C. Lee, J. F. Lin, A. J. Bard and C. B. Mullins, *J. Am. Chem. Soc.*, 2014, **136**, 2843–2850.
25 M. K. Bates, Q. Y. Jia, H. Doan, W. T. Liang and S. Mukerjee, *ACS Catal.*, 2016, **6**, 155–161.
26 D. Friebel, M. W. Louie, M. Bajdich, K. E. Sanwald, Y. Cai, A. M. Wise, M. J. Cheng, D. Sokaras, T. C. Weng, R. Alonso-Mori, R. C. Davis, J. R. Bargar, J. K. Norskov, A. Nilsson and A. T. Bell, *J. Am. Chem. Soc.*, 2015, **137**, 1305–1313.

27 H. F. Liang, F. Meng, M. Caban-Acevedo, L. S. Li, A. Forticaux, L. C. Xiu, Z. C. Wang and S. Jin, *Nano Lett.*, 2015, **15**, 1421–1427.
28 M. Bajdich, M. Garcia-Mota, A. Vojvodic, J. K. Norskov and A. T. Bell, *J. Am. Chem. Soc.*, 2013, **135**, 13521–13530.
29 M. Garcia-Mota, M. Bajdich, V. Viswanathan, A. Vojvodic, A. T. Bell and J. K. Norskov, *J. Phys. Chem. C*, 2012, **116**, 21077–21082.
30 I. C. Man, H. Y. Su, F. Calle-Vallejo, H. A. Hansen, J. I. Martinez, N. G. Inoglu, J. Kitchin, T. F. Jaramillo, J. K. Norskov and J. Rossmeisl, *ChemCatChem*, 2011, **3**, 1159–1165.
31 Y. G. Li, P. Hasin and Y. Y. Wu, *Adv. Mater.*, 2010, **22**, 1926–1929.
32 J. H. Yang and T. Sasaki, *Chem. Mater.*, 2008, **20**, 2049–2056.
33 M. Butel, L. Gautier and C. Delmas, *Solid State Ionics*, 1999, **122**, 271–284.
34 J. H. Huang, Q. C. Shang, Y. Y. Huang, F. M. Tang, Q. Zhang, Q. H. Liu, S. Jiang, F. C. Hu, W. Liu, Y. Luo, T. Yao, Y. Jiang, Z. Y. Pan, Z. H. Sun and S. Q. Wei, *Angew. Chem., Int. Ed.*, 2016, **55**, 2137–2141.
35 L. H. Hu, Q. Peng and Y. D. Li, *J. Am. Chem. Soc.*, 2008, **130**, 16136–16137.
36 J. W. Xiao, Q. Kuang, S. H. Yang, F. Xiao, S. Wang and L. Guo, *Sci. Rep.*, 2013, **3**, 2300.
37 X. W. Xie, Y. Li, Z. Q. Liu, M. Haruta and W. J. Shen, *Nature*, 2009, **458**, 746–749.
38 J. Yang, H. W. Liu, W. N. Martens and R. L. Frost, *J. Phys. Chem. C*, 2010, **114**, 111–119.
39 Y. C. Liu, J. A. Koza and J. A. Switzer, *Electrochim. Acta*, 2014, **140**, 359–365.
40 B. Gregoire, C. Ruby and C. Carteret, *Dalton Trans.*, 2013, **42**, 15687–15698.
41 B. S. Yeo and A. T. Bell, *J. Phys. Chem. C*, 2012, **116**, 8394–8400.
42 A. Ramirez, P. Hillebrand, D. Stellmach, M. M. May, P. Bogdanoff and S. Fiechter, *J. Phys. Chem. C*, 2014, **118**, 14073–14081.
43 M. Toupin, T. Brousse and D. Belanger, *Chem. Mater.*, 2004, **16**, 3184–3190.
44 J. C. Dupin, D. Gonbeau, P. Vinatier and A. Levasseur, *Phys. Chem. Chem. Phys.*, 2000, **2**, 1319–1324.
45 A. P. Grosvenor, M. C. Biesinger, R. S. Smart and N. S. McIntyre, *Surf. Sci.*, 2006, **600**, 1771–1779.
46 H. W. Nesbitt and D. Banerjee, *Am. Mineral.*, 1998, **83**, 305–315.
47 E. Rios, P. Chartier and J. L. Gautier, *Solid State Sci.*, 1999, **1**, 267–277.
48 J. Rosen, G. S. Hutchings and F. Jiao, *J. Catal.*, 2014, **310**, 2–9.
49 R. L. Doyle and M. E. G. Lyons, *Phys. Chem. Chem. Phys.*, 2013, **15**, 5224–5237.
50 Y. L. Deng, A. D. Handoko, Y. H. Du, S. B. Xi and B. S. Yeo, *ACS Catal.*, 2016, **6**, 2473–2481.
51 M. P. Browne, H. Nolan, G. S. Duesberg, P. E. Colavita and M. E. G. Lyons, *ACS Catal.*, 2016, **6**, 2408–2415.
52 R. L. Doyle and M. E. G. Lyons, *J. Electrochem. Soc.*, 2013, **160**, H142–H154.
53 J. R. Swierk, S. Klaus, L. Trotochaud, A. T. Bell and T. D. Tilley, *J. Phys. Chem. C*, 2015, **119**, 19022–19029.